ELECTROCHEMISTRY

O-coordinated W-Mo dual-atom catalyst for pH-universal electrocatalytic hydrogen evolution

Yang Yang^{1,2}*, Yumin Qian³*, Haijing Li⁴, Zhenhua Zhang⁵, Yuewen Mu², David Do⁶, Bo Zhou⁷, Jing Dong¹, Wenjun Yan⁸, Yong Qin⁸, Li Fang⁹, Renfei Feng¹⁰, Jigang Zhou¹⁰, Peng Zhang⁶, Juncai Dong⁴, Guihua Yu³, Yuanyue Liu³, Xianming Zhang^{1,11†}, Xiujun Fan^{1,11†}

Single-atom catalysts (SACs) maximize the utility efficiency of metal atoms and offer great potential for hydrogen evolution reaction (HER). Bimetal atom catalysts are an appealing strategy in virtue of the synergistic interaction of neighboring metal atoms, which can further improve the intrinsic HER activity beyond SACs. However, the rational design of these systems remains conceptually challenging and requires in-depth research both experimentally and theoretically. Here, we develop a dual-atom catalyst (DAC) consisting of O-coordinated W-Mo heterodimer embedded in N-doped graphene (W₁Mo₁-NG), which is synthesized by controllable self-assembly and nitridation processes. In W₁Mo₁-NG, the O-bridged W-Mo atoms are anchored in NG vacancies through oxygen atoms with W—O—Mo—O—C configuration, resulting in stable and finely distribution. The W₁Mo₁-NG DAC enables Pt-like activity and ultrahigh stability for HER in pH-universal electrolyte. The electron delocalization of W—O—Mo—O—C configuration provides optimal adsorption strength of H and boosts the HER kinetics, thereby notably promoting the intrinsic activity.

Copyright © 2020
The Authors, some rights reserved; exclusive licensee American Association for the Advancement of Science. No claim to original U.S. Government Works. Distributed under a Creative Commons Attribution NonCommercial License 4.0 (CC BY-NC).

INTRODUCTION

Electrochemical hydrogen evolution reaction (HER) provides a cost-efficient and sustainable method to generate H₂ effectively, which is an important component of developing green energy technologies (1). To date, Pt-based nanomaterials are widely considered as the state-of-the-art electrocatalysts for HER. However, the high cost and natural scarcity severely hamper their large-scale applications. Therefore, substantial efforts have been devoted to exploring cheap, efficient, and durable alternatives of Pt for hydrogen production. Recently, nonprecious metal-based catalysts have been studied extensively for HER such as carbides (2), nitrides (3), dichalcogenides (4), phosphides (5), and oxides (6); yet still, their HER activities and stabilities are far from satisfactory. In addition, to meet different applications, catalysts that function well over a wide pH range are highly regarded. For instance, water electrolyzers based on proton exchange membrane technology require catalysts operation in acidic solution; microbial electrolysis cells need catalysts that function well under neutral condition, and alkaline water electrolysis demands catalysts that operate in strongly basic media (7). Hence, designing and developing efficient, durable, and scalable HER catalysts working well in a pH-universal electrolysis system become important yet challenging.

The single-atom catalysts (SACs) maximize the efficiency of metal atoms utilization, enabling reasonable use of metal resources and achieving atomic economy, which is highly desirable for electrocatalysis (8). Unfortunately, the increased surface free energy renders SACs with only one kind of single metal site that tend to agglomerate, leading to a significant decline in performance. Compared to the single-atom components, the multiatom catalysts with tunable electronic environments could further improve the intrinsic activity and stability. In multiatom catalytic system, the metal cluster centers will offer a range of unique and often unexpected catalytic properties (9); the strong chemical interactions between neighboring atom-atom can efficiently stabilize the individual species and prevent agglomeration, thereby creating highly stable active sites. Within this context, dispersing metal atoms on support into a minimal cluster or dinuclear category could modulate the electronic structure by adjusting the ligand atom (10), coordination number (CN) (11), and structural distortion (12). In particular, the heteronuclear metal atom catalysis would optimize activity, stability, and selectivity through tuning metal active centers, which are not observable in their individual monometallic systems (13). Thus, it is very reasonable to expect that the dual-atom catalysts (DACs) with interacted biatomic metal cores could maximize the atom utilization and greatly improve the catalytic activity. However, synthesis and characterization of binuclear metal clusters remain a huge challenge, owing to the lack of atomic-scale control techniques under the harsh synthesis condition and the difficulty in identifying the exact noncrystallographic structures and active sites. Therefore, it is urgent and challenging to controllably synthesize DACs, as well as provide in-depth insight into the synthetic mechanism of heteronuclear species and the local environment associated with catalytic performance.

Polyoxometalates (POMs), a special class of metal oxide anion nanoclusters, feature stability, solubility, compatibility with nearly all other materials (i.e., supports, additives, and solvents), and diverse structural topologies, ensuring them attractive in broad fields of

¹Institute of Crystalline Materials, Shanxi University, Taiyuan, Shanxi 030006, China. ²Institute of Molecular Science, Shanxi University, Taiyuan, Shanxi 030006, China. ³Texas Materials Institute and Department of Mechanical Engineering, The University of Texas at Austin, Austin, TX 78712, USA. ⁴Beijing Synchrotron Radiation Facility, Institute of High Energy Physics, Chinese Academy of Sciences, Beijing 100049, China. ⁵Innovative Center for Advanced Materials, Hangzhou Dianzi University, Hangzhou, Zhejiang 310018, China. ⁶Department of Chemistry, Dalhousie University, Halifax, NS B3H 4R2, Canada. ⁷Institute of Microstructure and Properties of Advanced Materials, Beijing University of Technology, Chaoyang District, Beijing 100124, China. ⁸Analytical Instrumentation Center, Institute of Coal Chemistry, Chinese Academy of Sciences, Taiyuan 030001, China. ⁹College of Chemistry and Chemical Engineering, Shanxi University, Taiyuan, Shanxi 030006, China. ¹⁰Canadian Light Source, Saskatoon, SK S7N2V3, Canada. ¹¹School of Chemistry and Materials Science, Shanxi Normal University, Linfen, Shanxi 041001, China.

^{*}These authors contributed equally to this work.

[†]Corresponding author. Email: zhangxm@dns.sxnu.edu.cn (X.Z.); fxiujun@gmail.com (X.F.)

science. Moreover, the variable CN and geometry of POMs with separated units can inhibit agglomeration of metal atoms during the pyrolysis process. While Mo_7O_x clusters derived from POMs have been reported (14), they have not yet been explored to construct heteronuclear diatomic catalysts. Here, we report bimetallic DAC consisting of O-coordinated W-Mo heterodimer anchored in N-doped graphene (W₁Mo₁-NG); the W-O-Mo-O-C configuration of which is distinct from the reported dual-metal sites using traditional methods. The W- and Mo-based POMs are used as precursors for producing W-Mo DAC, which is prepared through a hydrothermal reaction followed by chemical vapor deposition (CVD) process. In W₁Mo₁-NG, heteronuclear W-Mo dual atoms are immobilized in the NG vacancies and stabilized through W-O and Mo-O bonds. The W and Mo atoms are respectively located in oxygen-bridged [WO₄] tetrahedron and distorted [MoO₆] octahedron units; W atom is bridged with Mo atom via O atom, functioning as a bimetallic dimer environment. The distinctive W-O-Mo-O-C configuration with strong covalent interactions works as stable and excellent catalyst toward HER in pH-universal electrolysis. The electron delocalization of O-coordinated W-Mo heterodimer results in a favorable adsorption behavior of H and improved HER kinetics, ultimately enhancing the intrinsic activity.

RESULTS

W₁Mo₁-NG DAC

W₁Mo₁-NG electrocatalyst was synthesized through a three-step procedure, as schematically illustrated in Fig. 1A. A precursor solution was first prepared by sonicating tungstic acid, molybdate, and graphene oxide (GO) in water. The Na₂WO₄·2H₂O and (NH₄)₆Mo₇O₂₄·4H₂O were selected as W and Mo sources, respectively. The well-mixed precursor solution was then subjected to a hydrothermal treatment, in which paired W-Mo species were formed and anchored into partially reduced GO (p-RGO). Subsequently, the homogeneous mixture was freeze-dried to minimize restacking of p-RGO sheets. Last, the W₁Mo₁-NG DAC was obtained with CVD treatment in the NH₃/Ar gas at 800°C. For comparison, a series of DACs with various CVD times and molar ratios of W/Mo (table S1), together with homonuclear diatomic Mo and W supported on NG (denoted as Mo₂-NG and W₂-NG, respectively), were also synthesized. Further details of the experiments were provided in Materials and Methods.

The formation mechanism of W₁Mo₁-NG DAC was based on POMs self-assembly chemistry. Specifically, Na₂WO₄·2H₂O and (NH₄)₆Mo₇O₂₄·4H₂O were added to GO suspension (Fig. 1B, 1) in an ultrasonic bath (pH 6.1 to pH 6.3). Afterward, in the hydrothermal process, protonation of carboxyl anion occurred (Fig. 1B, 2), followed by the removal of protonated carbonyl and epoxy on GO (Fig. 1B, 3); the delocalized π -electron system and H⁺ underwent protonation to obtain positively charged p-RGO (Fig. 1B, 4) (15). In a mild acidic solution, protonation promoted Mo(VI) oxo in MoO₄²⁻ fragment transformed to Mo hydroxo and lastly to Mo aquo ligands ([MoO₄(H₂O)₂]²⁻) (16), while the hydrogentungstate anion ([WO₃(OH)]⁻) from WO₄²⁻ fragment retained the tetrahedral coordination (17). Hence, heteronuclear W-Mo species could be obtained through self-assembly of [WO₃(OH)]⁻ and [MoO₄(H₂O)₂]²⁻ with dehydration condensation reaction; before aggregation and rearrangement, the heteronuclear W-Mo species could be captured and stabilized with protonated p-RGO sheets as counterion (Fig. 1B, 5) (18). Because of the intensive coupling of negatively charged W-Mo

dimer anions and positively charged protonated p-RGO sheets, the O-coordinated W-Mo heterodimers could be electrostatically attracted onto the p-RGO sheets without any additives. As a result, the hydrothermal self-assembly process created a tremendous opportunity for heteronuclear W-Mo dual atoms to anchor in p-RGO through strong covalent interactions. Where small amount of low-nuclear $MM'O_x$, MMO_x , and $M'M'O_x$ (M, M' = Mo, W) clusters could also formed. Last, uniform W₁Mo₁-NG DAC (Fig. 1B, 6) was prepared by ammonia annealing. During CVD process, further reduction of p-RGO and N doping occurred simultaneously. The successful synthesis of W₁Mo₁-NG DAC is contributed to the structural asymmetry between the protonated p-RGO sheets and metal precursors in mild acidic solution, in which protonated p-RGO sheets working as counterion inhibit WO₄²⁻ and MoO₄²⁻ fragments aggregating into block materials (19). The general synthetic strategy of heteronuclear DAC can also be extended to other POM systems, such as vanadium, niobium, and tantalum, which provides an alternative way to develop atomically dispersed catalysts with higher complexity.

Structural characterization of W₁Mo₁-NG DAC

The morphology and structure of W₁Mo₁-NG were initially investigated by scanning electron microscopy (SEM), transmission electron microscopy (TEM), and aberration-corrected high-angle annular dark-field scanning TEM (AC HAADF-STEM). As revealed in Fig. 2A and fig. S1, W₁Mo₁-NG and RGO have similar morphology with abundant wrinkles and ripples, which serve as anchoring sites to stabilize the metallic species. No nanoparticles or clusters are observed in the brightfield TEM image (Fig. 2B). The AC HAADF-STEM image (Fig. 2C) presents high density of small bright dots, validating that the W-Mo species are atomically distributed on NG. Furthermore, the magnified AC HAADF-STEM image clearly demonstrates the existence of a large proportion of isolated heteronuclear W-Mo atoms (marked with circles, Fig. 2D). Apart from the dominant amount of W-Mo dual atoms, a few small clusters are also observed (fig. S2). The statistical analysis of 100 pairs of heteronuclear W-Mo atoms shows that the W-Mo distance is below 3.6 Å (Fig. 2E), which is conspicuously longer than the Mo–Mo/ W—Mo/W—W bonds (ca. 3.0 Å) in metals bulk, indicating that the W and Mo atoms are bridged via extra atoms. In W₁Mo₁-NG, the coaxial line of W and Mo atoms may not be parallel to the NG plane due to the wrinkles in NG, resulting in variable W-Mo diatomic distances in HAADF images. Figure 2F is a simplified and intuitive depiction of the dizygotic W-Mo atoms anchoring in NG and exhibits the W-Mo distance in regions 1 to 3 of Fig. 2D. The heteronuclear W-Mo atoms can be clearly distinguished by intensity; the distances shown in the intensity profiles are consistent with the projection spacing of W-Mo atoms on the visual plane. The energy-dispersive x-ray spectroscopy (EDS) mapping analysis reveals the homogeneous distribution of C, N, O, Mo, and W elements (Fig. 2G and fig. S3). Simultaneously, the HAADF images of Mo₂-NG and W₂-NG also clearly reveal the homonuclear Mo2 and W2 atoms anchored in NG sheets, respectively (figs. S4 and S5). The above results demonstrate that the hydrothermal and CVD methods effectively create high-density heteronuclear W-Mo atoms distributed on pleated NG sheets.

To gain insights into the chemical composition and the valence states of W_1Mo_1 -NG DAC, we carried out Raman spectrum, x-ray diffraction (XRD), and x-ray photoelectron spectroscopy (XPS) measurements. As exhibited in Raman spectra (Fig. 3A), the intensity

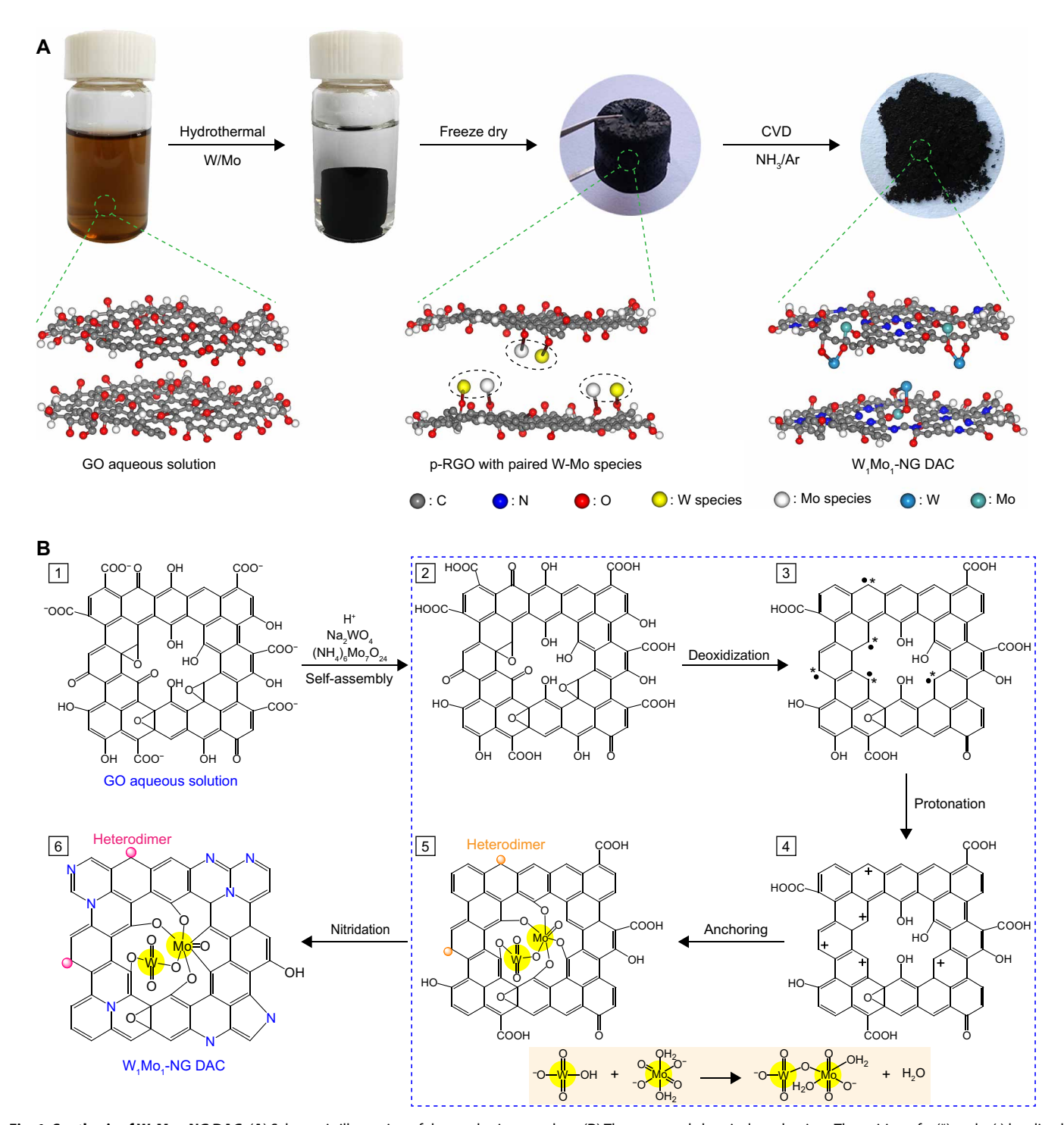


Fig. 1. Synthesis of W_1Mo_1 -NG DAC. (A) Schematic illustration of the synthetic procedure. (B) The proposed chemical mechanism. The pairing of σ (*) and π (•) localized electrons at the zigzag sites is indicated.

ratio of D band to G band (I_D/I_G) for W_1Mo_1 -NG (1.16) is higher than that of NG (1.05), which indicates that structural defects are introduced into W_1Mo_1 -NG. Furthermore, the Brunauer-Emmett-Teller surface areas of W_1Mo_1 -NG and NG are 566 and 268 m² g⁻¹, respectively (Fig. 3B), and the main pore size is centered at 3.5 nm (Fig. 3B, inset). These results suggest that the interacted W and Mo

atoms can effectively inhibit the agglomeration of NG sheets and generate a considerable amount of voids (fig. S6), which provides nucleation sites for W-Mo heterodimers. The defective W_1Mo_1 -NG with porous structure and large surface area can effectively promote the electrolyte permeation and charge transfer. In XRD patterns, no diffraction peaks of metal-based crystalline phases in DACs, such as

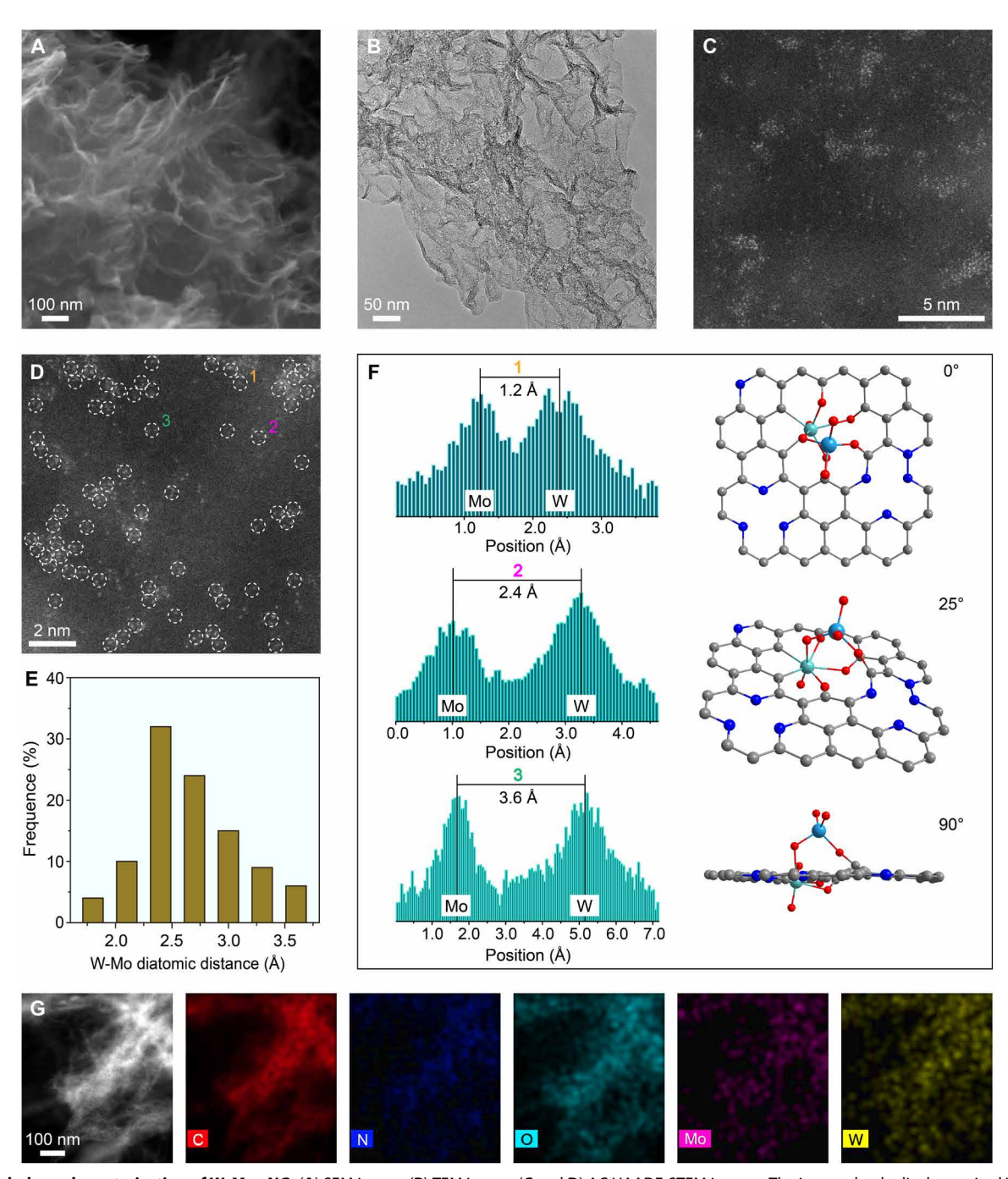


Fig. 2. Morphology characterization of W₁Mo₁-NG. (A) SEM image. (B) TEM image. (C and D) AC HAADF-STEM images. The image clearly displays paired W-Mo atoms (white circles). (E) Statistical W-Mo diatomic distance in AC HAADF-STEM images. (F) Intensity profiles obtained in areas 1 to 3 and the corresponding schematics show different W-Mo projection distances on the visual plane. For top, middle, and bottom schematics, tilt angles of NG plane relative to the visual plane are 0°, 25°, and 90°, respectively. Atom colors: royal blue, W; cyan, Mo; dark gray, C; blue, N; red, O. (G) HAADF-STEM image and corresponding EDS elemental mapping images.

unary W- or Mo-based carbides/nitrides/oxides, are detected (Fig. 3C). However, XPS survey spectrum confirms that W_1Mo_1 -NG consists of W, Mo, N, O, and C elements (Fig. 3D), consistent with the EDS elemental mapping (Fig. 2G). The atomic concentrations of W and Mo in W_1Mo_1 -NG determined by XPS are 0.38 and 0.36 atomic %, respectively, which are close to the inductively coupled plasma mass spectrometry (ICP-MS) results [5.01 and 2.55 weight % (wt %),

respectively] (table S2). Notably, all these DACs have relatively high metal loading of 7.5 wt %, which could not be achieved with conventional deposition-reduction method (13). The Mo 3d XPS of W_1Mo_1 -NG shows two peaks at 235.6 and 232.4 eV (Fig. 3E), corresponding to Mo $3d_{3/2}$ and Mo $3d_{5/2}$ core energy levels, respectively, validating the presence of Mo(VI) (20). For W 4f XPS (Fig. 3F), W ions have two well-defined peaks at 37.5 and 35.3 eV in W_1Mo_1 -NG

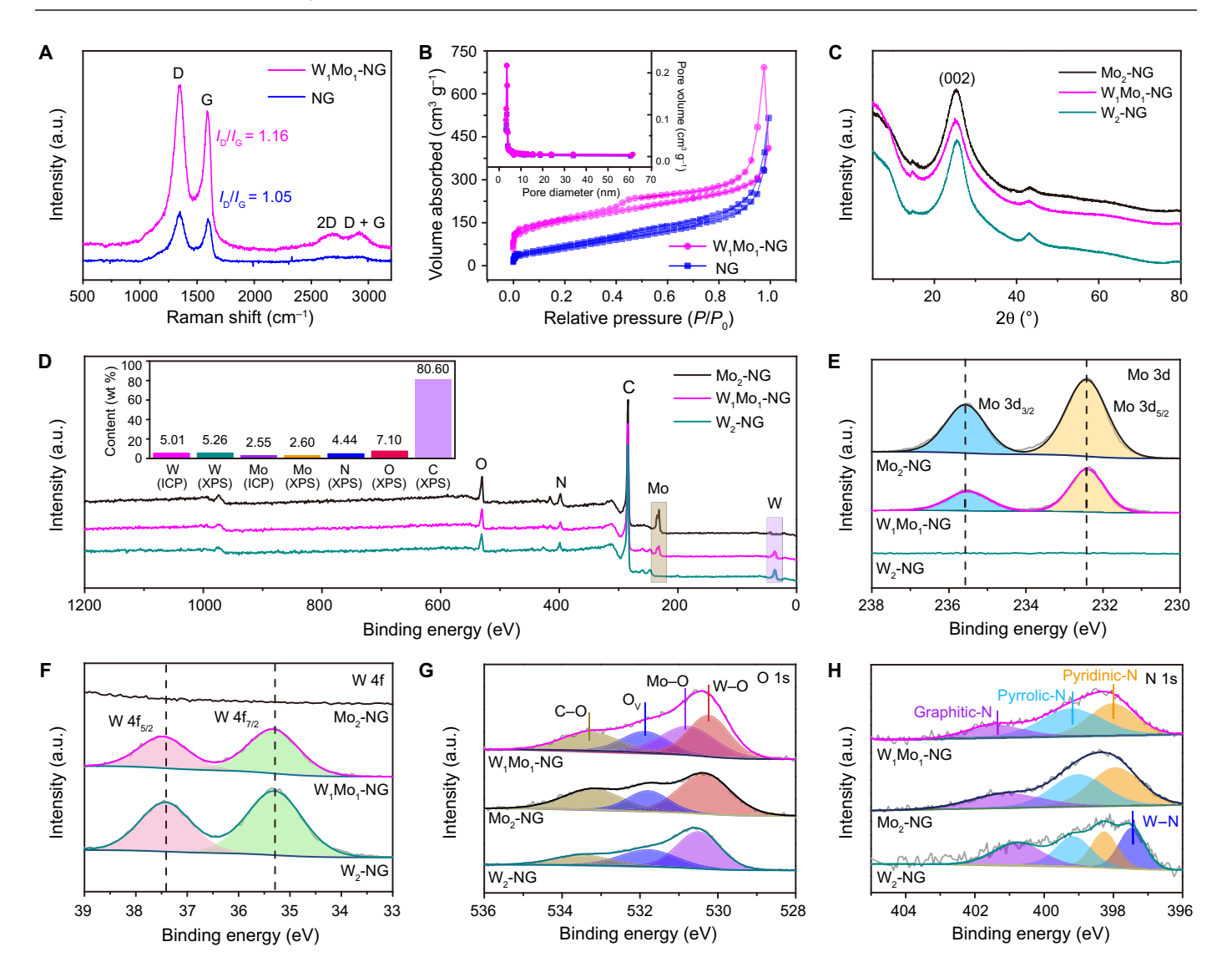


Fig. 3. Compositional characterization. (**A**) Raman spectra of W_1Mo_1 -NG and NG. The two-dimensional (2D) peak is obviously enhanced in W_1Mo_1 -NG, demonstrating that the number of graphene layers is reduced compared to raw NG. The appearance of D+G band at 2922 cm⁻¹ declares the increased structure disorder. a.u., arbitrary units. (**B**) N_2 adsorption-desorption isotherm; inset is pore size distribution diagram. (**C**) XRD patterns. The weak diffraction peaks at 14.6° and 43.1°, respectively, demonstrate the presence of oxygen-containing functional groups and a short-range order in stacked graphene layers. (**D**) XPS survey spectra. The W is absent in Mo_2 -NG, and Mo is absent in W_2 -NG. Inset is the percentages of W, Mo, N, O, and C in W_1Mo_1 -NG measured by XPS and ICP-MS. High-resolution (**E**) Mo 3d and (**F**) W 4f XPS spectra. (**G**) O 1s spectra of Mo_2 -NG, W_1Mo_1 -NG, and W_2 -NG. The fitted peak at 533.2 eV can be assigned to C—O bond. (**H**) High-resolution N 1s spectra of W_1Mo_1 -NG, Mo_2 -NG, and W_2 -NG, and W_2 -NG.

ascribed to the W $4f_{5/2}$ and W $4f_{7/2}$, respectively, being consistent with high oxidation state of W(VI) (21). The Mo 3d in W₁Mo₁-NG has some shift toward low binding energy compared to Mo₂-NG, whereas the W 4f in W₁Mo₁-NG shifts positively relative to W₂-NG. These microdisplacements indicate the altering of local electronic structure for heteronuclear W₁Mo₁-NG system, which could be attributed to the structural perturbation of W-Mo heterodimers. Moreover, the control samples with various ratios of W/Mo and CVD times were also subjected to XPS measurements. For Mo 3d and W 4f spectra, the varying metal ratio triggers an electron transfer at a certain CVD time (fig. S7), while adjusting the CVD time with a fixed metal ratio does not introduce any changes (fig. S8). As a result, the local electronic structure of W-Mo heterodimers can be effectively modulated via adjusting the ratio of W/Mo. As revealed in Fig. 3G, the deconvoluted peaks around 530.2 and 530.8 eV are

assigned to Mo—O and W—O bonds (22, 23), respectively, further confirming that W-Mo heterodimers are O-coordinated within W₁Mo₁-NG; the peak around 532.0 eV derives from oxygen vacancy (O_v) (24). Notably, peak areas of O_v are different; W₁Mo₁-NG has higher O_v concentration than single metal—doped Mo₂-NG and W₂-NG, in accordance with the electron paramagnetic resonance spectra (fig. S9). Because the oxygen-containing functional groups are easily detached from fluffy NG during CVD process, the concentration of O_v may be positively correlated with the specific surface area. Meanwhile, the N 1s spectra are deconvoluted into three characteristic peaks of pyridinic-N (398.0 eV), pyrrolic-N (399.2 eV), and graphitic-N (401.4 eV) species (Fig. 3H), demonstrating the NG, while W—N bond only appears in W₂-NG, suggesting W atoms coordinating with N atoms. Metal carbides are absent in the C 1s spectra of DACs (fig. S10). Distinctly, the metal centers in

 W_1Mo_1 -NG and Mo_2 -NG are O-coordinated, while the W(VI) in W_2 -NG are co-coordinated with O and N atoms.

To probe the local coordination chemistry of DACs, we conducted x-ray absorption near-edge structure (XANES) and extended x-ray absorption fine structure (EXAFS). In the Mo K-edge XANES (Fig. 4A), W₁Mo₁-NG and Mo₂-NG exhibit a shoulder peak (■) in the pre-edge region, suggesting the formation of distorted [MoO₆] octahedron with Mo=O bond (25). Moreover, according to the linear relationship between the Mo oxidation state and the energy position (\blacklozenge) (26), the average oxidation state of Mo ions in W₁Mo₁-NG and Mo2-NG is close to 6, which matches well with the XPS results (Fig. 3E). Figure 4B shows the k^3 -weighted Fourier transform (FT)– EXAFS spectra at Mo K-edge. As expected, W₁Mo₁-NG and Mo₂-NG have two strong peaks at 1.25 and 1.88 Å, which could be attributed to Mo=O and Mo-O bonds, respectively. Comparing with Mo foil, no apparent peaks (2.43 and 2.96 Å) for Mo-Mo bonds are detected in both W₁Mo₁-NG and Mo₂-NG, confirming the absence of Mo nanoparticles, in line with the STEM observation. For the W L₃-edge XANES spectra, the oxidation state of W ions in W₁Mo₁-NG and W₂-NG is higher than W powder but lower than WO₃ (Fig. 4C). The primary peak around 10,210 eV is attributed to the electronic transition from $2p_{3/2}$ to unoccupied 5d orbital (27). In comparison with W2-NG, W1Mo1-NG exhibits higher intensity of white line, which demonstrates the electron deficiency at W atoms by introducing Mo atoms, suggesting strong interactions between heteronuclear W-Mo atoms and NG support. Furthermore, the main peak of W₁Mo₁-NG (10,210.12 eV) moves toward low energy compared to W₂-NG (10,210.71 eV) and WO₃ (10,210.74 eV), revealing the low CN environment of W atoms in W₁Mo₁-NG (28). As displayed in the FT-EXAFS spectra at W L₃-edge (Fig. 4D), W₁Mo₁-NG and W2-NG have only one prominent peak located at 1.36 Å assigned to the W—O coordination. The weak peaks at 2.86 and 3.20 Å correspond to the W-Mo and W-W contributions for W₁Mo₁-NG and W2-NG, respectively, indicating that W atoms within W1Mo1-NG and W2-NG are atomically distributed. To confirm the adjacent properties of the metal atoms, we conducted wavelet transform (WT)-EXAFS. As shown in Fig. 4E, the WT signal related to Mo—Mo bond in Mo foil is not detected in both W₁Mo₁-NG and Mo₂-NG, further confirming the absence of Mo-containing nanoparticles. Compared to MoO₃, W₁Mo₁-NG and Mo₂-NG show two intensity maxima at 3.9 and 9.3 Å⁻¹, which are respectively associated with the Mo-O and Mo-O-W/Mo paths, consistent with the Mo K-edge FT-EXAFS results. For WT-EXAFS at W L₃-edge (Fig. 4F), W₁Mo₁-NG and W₂-NG display the intensity maxima at 4.1 and 3.9 Å⁻¹ for W—O and W—O/N paths, respectively, which are close to the W-O bond (4.2 Å⁻¹) in WO₃ reference, but distinct from the W-W bond (7.3 Å⁻¹) of W powder. Moreover, WT signal at 9.2 Å⁻¹ of W₁Mo₁-NG and W₂-NG should be derived from the W-O-Mo and W-N/O-W contributions, respectively. Unambiguously, by combining the WT results at Mo K-edge and W L3-edge, the metal atoms are confirmed to be bridged via extra O or N atoms in the W₁Mo₁-NG, Mo₂-NG, and W₂-NG. To determine the configuration of these DACs, we used density functional theory (DFT) calculations to deduce the bimetal models based on the FT-EXAFS experimental spectra and fitted curves. The EXAFS fitting results exhibit that the Mo atom has four coordinating interactions of Mo \rightleftharpoons O (1.79 Å), Mo-O (1.99 Å), Mo-C/N (2.66 Å), and Mo-W (3.29 Å) and the corresponding CN values are 1.9, 2.2, 1.1, and 0.9, respectively (table S3). Meanwhile, the four coordination paths of W atom at 1.83, 2.01, 2.67, and 3.29 Å are respectively assigned to W=O, W-O, W-C/N, and W-Mo with corresponding CN of 2.1, 1.7, 1.2, and 1.1 (table S4). The EXAFS fitting curves at *R*-space and *k*-space are consistent well with experiment spectra of W₁Mo₁-NG (Fig. 4, G and H). Then, possible W-Mo heterodimer models were constructed and optimized with DFT calculations based on the coordination environment (fig. S11). For the O-coordinated W₁Mo₁-NG model (Fig. 4G, inset), the W=O, Mo=O, and O-bridged W-Mo paths length are 1.75, 1.71, and 3.54 Å (fig. S12), respectively, in good agreement with EXAFS fitting data (1.79, 1.79, and 3.29 Å, respectively). As a result, the geometry of heteronuclear W-Mo atoms anchored in NG vacancy by four O atoms and two C atoms is the most possible actual configuration. Wherein one W atom binding with O atom to form W-O motif, which further binds with a neighboring Mo atom to form a W-O-Mo-O-C configuration, while the W and Mo atoms respectively exist in the [WO₄] tetrahedron and distorted [MoO₆] octahedron units. Quantitative EXAFS fitting results for homonuclear systems are also summarized in Fig. 4, I and J and fig. S13. Note that the local coordination of Mo atom in Mo₂-NG resembles that of W₁Mo₁-NG, suggesting similar local environment around the Mo center, while for W₂-NG, the CN of the W-O/N path (second shell) is 2.3, which is higher than that of W₁Mo₁-NG (1.7). According to the EXAFS fitting and DFT calculation results, the homonuclear Mo₂ and W₂ dual atoms are determined to be inlaid in NG with seven O and N atoms, respectively (fig. S14). Other coordination configurations are excluded by comparing the EXAFS fitting and XPS results (fig. S15). Compared to homonuclear Mo₂-NG and W₂-NG, the coaxial line of W-Mo atoms is not parallel to the NG plane, which gives rise to structural deformation. The structural perturbation of W-Mo heterodimers can effectively modulate the electronic structure of the W, Mo, and O atoms in the defective NG, ensuring high intrinsic activity. Obviously, the paired metal atoms in W₁Mo₁-NG (W-O-Mo-O-C) and Mo₂-NG (Mo-O-Mo-O-C) are anchored in NG by O atoms, while paired W atoms in W₂-NG (W—N—W—N—C) are anchored in NG by N atoms. Usually, the metal atoms are dispersed on N-doped carbon support in SACs with form of M-N-C (M refers to transition metals). Unambiguously, the bulk oxides of W and Mo can be converted to the corresponding nitrides in an NH₃ atmosphere at high temperature (29). In this work, the energy provided during the CVD process probably fails to reach the dissociation energy of M-O bonds (M = W, Mo) in W-Mo and Mo₂ dimers obtained via hydrothermal process, thus keeping M-O coordination. For the tungstate system, the structural stability of isolated dinuclear tungsten oxide is extremely poor (30), so that the weaker W-O bond cannot survive in the high temperature CVD process compared to W-N bond. Consequently, we have prepared DAC with W-O-Mo-O-C configuration through facile selfassembly of W- and Mo-based POMs, followed by CVD procedure. In W₁Mo₁-NG, the O-coordinated W-Mo heterodimer with distorted structure provides the possibility to modulate the electronic structure around the W, Mo, and O atoms, thereby improving the electrocatalytic activity.

Electrocatalytic HER performance

The HER performance of DACs was investigated in $0.5~M~H_2SO_4$ and 1.0~M~KOH solutions using a standard three-electrode setup. All potentials were referenced to a reversible hydrogen electrode (RHE) and without iR compensation. The commercial Pt/C and raw NG were tested for comparison. As illustrated in Fig. 5A, W_1Mo_1 -NG

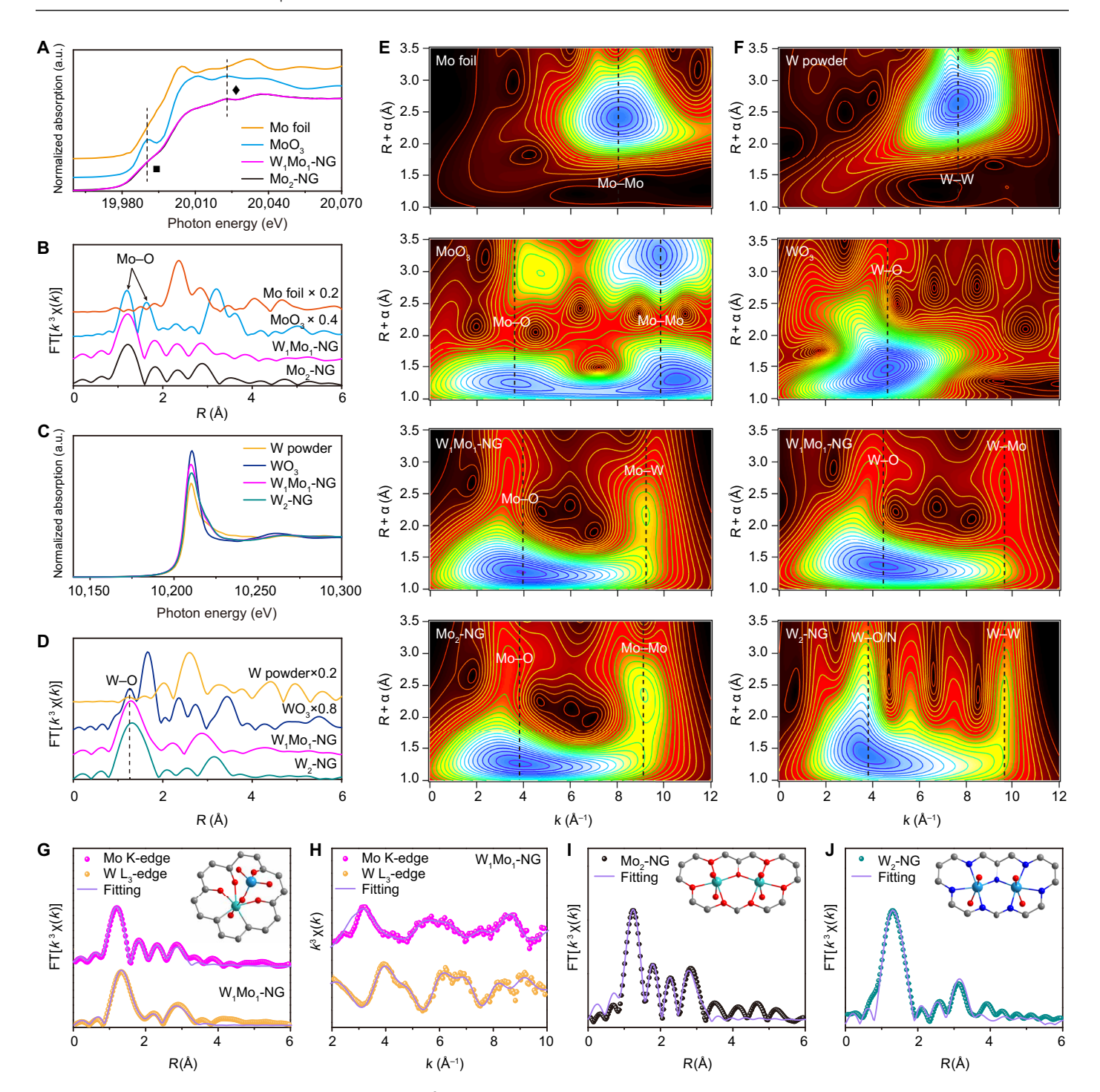


Fig. 4. X-ray absorption characterization. (**A**) XANES and (**B**) k^3 -weight FT-EXAFS spectra of W₁Mo₁-NG, Mo₂-NG, and the reference samples at Mo K-edge. (**C**) XANES and (**D**) FT-EXAFS spectra of W₁Mo₁-NG, W₂-NG, W powder, and WO₃ at W L₃-edge. The W ions in WO₃ are in a [WO₆] octahedron environment. WT-EXAFS of W₁Mo₁-NG, Mo₂-NG, W₂-NG, and the references at (**E**) Mo K-edge and (**F**) W L₃-edge. (**G** and **H**) The corresponding Mo K-edge and W L₃-edge EXAFS fitting curves for W₁Mo₁-NG at *R*-space and *k*-space, respectively. (**I**) The corresponding Mo K-edge EXAFS fitting curve for W₂-NG at *R*-space. The insets of (G), (I), and (J) are the schematic models of W₁Mo₁-NG, Mo₂-NG, and W₂-NG, respectively. Atom colors: royal blue, W; cyan, Mo; dark gray, C; blue, N; red, O.

exhibits excellent catalytic activity toward HER, giving a near-zero onset potential ($U_{\rm onset}$) in acidic electrolyte. As a consequence of polarization, W₁Mo₁-NG produces cathodic geometric current density (j) of 10 mA cm⁻² at an overpotential of 24 mV (η_{10} = 24 mV), which

is much lower than those of Mo₂-NG (145 mV), W₂-NG (156 mV), raw NG (200 mV), and other counterparts (fig. S16). Impressively, W₁Mo₁-NG delivers a high cathode current density at overpotential (η) above 50 mV, which is even superior to that of commercial Pt/C

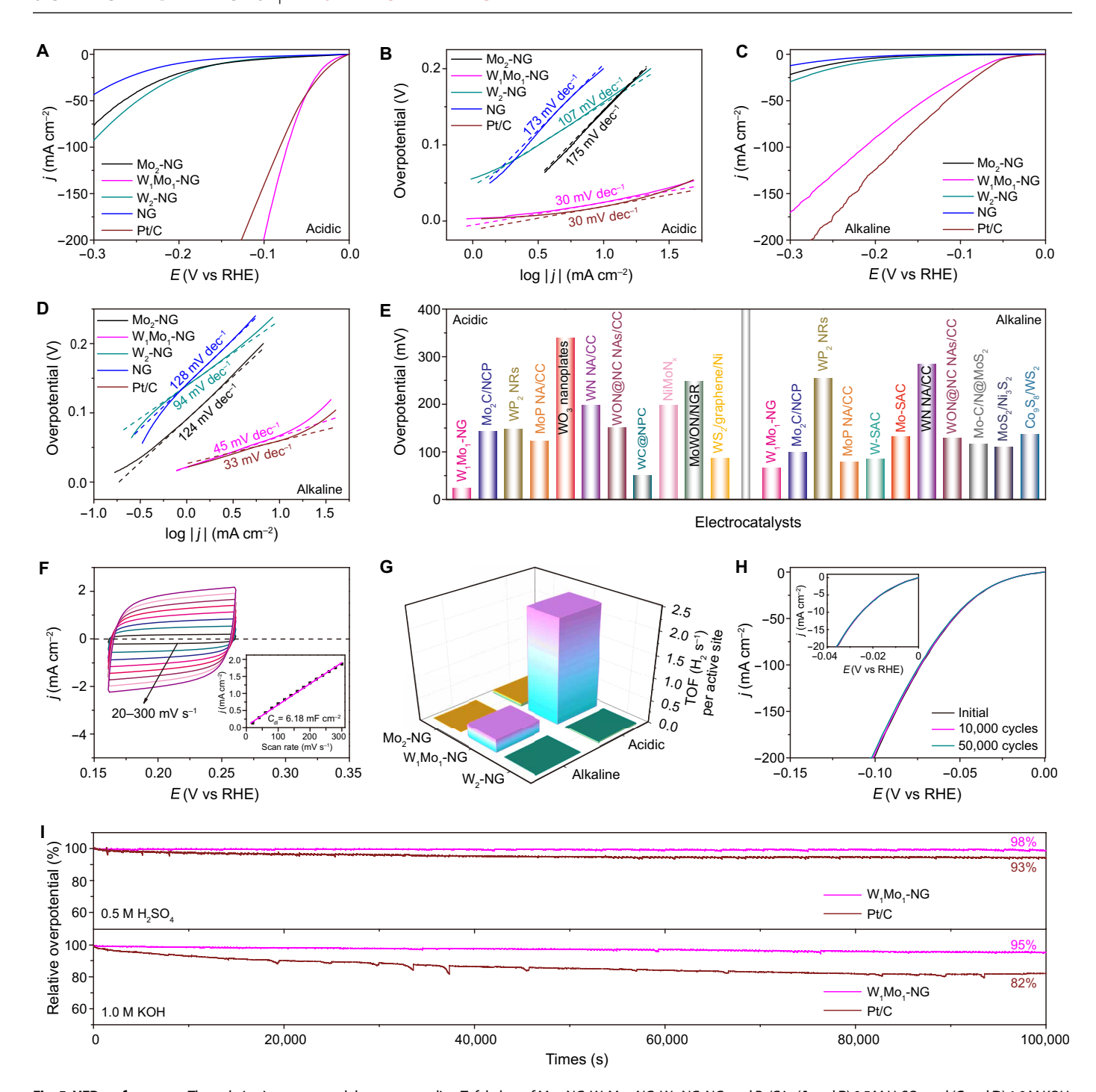


Fig. 5. HER performance. The polarization curves and the corresponding Tafel plots of Mo₂-NG, W₁Mo₁-NG, W₂-NG, NG, and Pt/C in (**A** and **B**) 0.5 M H₂SO₄ and (**C** and **D**) 1.0 M KOH, respectively. (**E**) Comparison of the η_{10} in 0.5 M H₂SO₄ and 1.0 M KOH solutions for W₁Mo₁-NG and reported W- and Mo-based HER electrocatalysts. (**F**) Cyclic voltammetry (CV) cycles for W₁Mo₁-NG with varying scan rates from 20 to 300 mV s⁻¹; the inset is C_{dl} measurement in 1.0 M KOH. (**G**) Turnover frequency (TOF) values of Mo₂-NG, W₁Mo₁-NG, and W₂-NG in 0.5 M H₂SO₄ and 1.0 M KOH solutions, respectively. (**H**) Polarization curves recorded from W₁Mo₁-NG catalyst before and after 50,000 potential cycles in 0.5 M H₂SO₄. (**I**) Galvanostatic responses recorded on W₁Mo₁-NG and Pt/C at a cathodic current density of 10 mA cm⁻² under acidic and alkaline solutions.

catalyst. Distinctly, this overpotential ($\eta_{10} = 24 \text{ mV}$) is the lowest among the reported earth-abundant HER catalysts, such as CoP/NiCoP nanotadpoles (125 mV) (31), Ni₂P/Ni@C (149 mV) (32), and Fe₃C-Co/NC (298 mV) (2), as well as other catalysts (table S5). Specifically, W₁Mo₁-NG affords a small Tafel slope of 30 mV dec⁻¹, which is much

lower than those of Mo₂-NG (175 mV dec⁻¹), W₂-NG (107 mV dec⁻¹), and NG (173 mV dec⁻¹) (Fig. 5B), reflecting that W₁Mo₁-NG has highest HER kinetic process through the Volmer-Tafel mechanism and the surface recombination step is the rate-limiting step (33). The exchange current density (j_0) of W₁Mo₁-NG is calculated

to be 1.78 mA cm⁻², which is much higher than those of Mo₂-NG $(1.50 \text{ mA cm}^{-2})$, W₂-NG $(0.33 \text{ mA cm}^{-2})$, and NG $(0.67 \text{ mA cm}^{-2})$ (fig. S17). Distinctly, W₁Mo₁-NG has such a lower Tafel slope and larger j_0 value than those of Mo₂-NG, W₂-NG, and raw NG, suggesting the superior HER kinetics and enhancing the intrinsic activity of W₁Mo₁-NG. In addition, in alkaline electrolyte (Fig. 5, C and D), W_1Mo_1 -NG exhibits a small U_{onset} of -26 mV, upon which the cathodic current density elevates substantially at more negative potentials; W_1Mo_1 -NG delivers η_{10} of 67 mV, which is much lower than those of Mo₂-NG (247 mV), W₂-NG (223 mV), NG (281 mV), other counterparts, and reported transition metal-based HER catalysts (fig. S18 and table S6). The Tafel slope of W₁Mo₁-NG is 45 mV dec^{-1} , which is lower than those of Mo₂-NG (124 mV dec⁻¹), W_2 -NG (94 mV dec⁻¹), and NG (128 mV dec⁻¹). Similarly, the j_0 of W₁Mo₁-NG is calculated to be 0.26 mA cm⁻², which is much higher than those of Mo_2 -NG (0.19 mA cm⁻²), W_2 -NG (0.04 mA cm⁻²), and NG (0.08 mA cm⁻²) (fig. S19). The results reveal that W_1Mo_1 -NG has more favorable HER kinetics than Mo2-NG, W2-NG, and NG under both acidic and alkaline media. We further compared the HER activity with recently reported tungsten and molybdenum electrocatalysts (Fig. 5E). It is evident that W₁Mo₁-NG DAC requires the lowest η₁₀ (24 and 67 mV, respectively) in 0.5 M H₂SO₄ and 1.0 M KOH, outperforming almost all W- and Mo-based HER catalysts. In addition, the electrochemical double-layer capacitance (C_{dl}) was measured by performing cyclic voltammetry (CV) at various scan rates (Fig. 5F). W₁Mo₁-NG has the C_{dl} values of 7.20 and 6.18 mF cm⁻², which are better than those of Mo₂-NG (5.26 and 4.15 mF cm⁻²), W₂-NG (6.01 and 4.72 mF cm⁻²), and NG (2.06 and 1.80 mF cm⁻²) in 0.5 M H₂SO₄ and 1.0 M KOH solutions, respectively (figs. S20 and S21), suggesting that the heteronuclear W₁Mo₁-NG system can subjoin active surface area (22). Furthermore, geometric current density has been widely used to evaluate the activity of electrocatalysts. However, there is considerable dispute on its effectiveness especially in the case of highly porous electrocatalysts (5). To exclude the effect of surface area and compare the intrinsic HER activity, geometric current density was normalized by electrochemical active surface area (ECSA; j_{ECSA}) and to further identify the catalysts's intrinsic activity. As shown in fig. S22, W_1Mo_1 -NG delivers the j_{ECSA} values of 1100.49 and 165.00 μ A cm⁻² at $\eta = 100$ mV, which are markedly higher than those of Mo₂-NG (32.28 and 11.50 μA cm⁻²), W₂-NG (34.40 and 3.63 μA cm⁻²), NG (46.60 and 11.83 μA cm⁻²), and Pt/C (262.82 and 69.64 μA cm⁻²) in 0.5 M H₂SO₄ and 1.0 M KOH solutions, respectively. These reveal that W₁Mo₁-NG has better intrinsic activity than Mo₂-NG, W₂-NG, and NG, even outperforming benchmark Pt/C in pH-universal electrolyte (8).

In addition, to gain further insight into the intrinsic catalytic activity, we measured the turnover frequency (TOF) per active site. Thus, the number of active sites was titrated from integrated charge of anodic CV cycles at phosphate buffer solution (pH 7) (fig. S23) (34). Evidently, W₁Mo₁-NG affords the highest TOF values of 2.36 and 0.42 H₂ s⁻¹ at $\eta = 100$ mV, which are about 59, 42, and 26, 21 times higher than those of Mo₂-NG (0.04 and 0.01 H₂ s⁻¹) and W₂-NG (0.09 and 0.02 H₂ s⁻¹) in 0.5 M H₂SO₄ and 1.0 M KOH, respectively (Fig. 5G). The results indicate that heteronuclear W₁Mo₁-NG system delivers prominent catalytic hydrogen production capacity compared to homonuclear Mo₂-NG and W₂-NG. This superior catalytic performance is related to the distinctive W—O—Mo—O—C configuration, which provides a unique electronic structure and improves electrical conductivity, notably affecting on the electron

transfer from the catalyst surface to adsorbed species (35). Besides, electrochemical impedance spectroscopy (EIS) technique was also performed. Among them, W₁Mo₁-NG DAC yields small charge-transfer resistance (R_{ct}) (1 and 2 ohms) in 0.5 M H₂SO₄ and 1.0 M KOH, which are much lower than those of Mo₂-NG (5 and 5 ohms), W₂-NG (4 and 10 ohms), and NG (40 and 20 ohms), respectively (fig. S24). The Mo₂-NG and W₂-NG both exhibit lower R_{ct} than that of raw NG, indicating that the foreign metal atoms doping facilitate electron transport at the electrode/electrolyte interface. Notably, the HER performance of W₁Mo₁-NG catalyst is extremely superior to Mo₂-NG and W₂-NG, which can be attributed to the atomic W-O-Mo-O-C moiety having favorable local electronic structure. Here, the highest performance of W₁Mo₁-NG is achieved with feed molar ratio for W/Mo of 7:13 at CVD processing time of 3 hours, indicating that the synergy of W and Mo species decreases the reaction kinetic barrier for HER. Since the self-assembly of POMs strongly depended on the pH and the concentration of metal precursors, W₁Mo₁-NG heterocatalysts with W/Mo molar ratio of 1:1 are successfully synthesized with feed molar ratio for W/Mo of 7:13, based on XPS, ICP-MS, x-ray absorption, and DFT results. When the feed molar ratio of W/Mo precursors is 1:1, the loadings of W and Mo atoms in the catalyst are 6.82 and 1.02 wt %, respectively (table S2). Under this condition, the paired W-Mo atoms are not dominant amount, which weakens the synergistic effect of W and Mo atoms and reduces HER activity. As a result, the optimal performance in HER is achieved on W₁Mo₁-NG with electron delocalization of paired W-Mo atoms.

The stability and durability of W₁Mo₁-NG were further analyzed. As illustrated in Fig. 5H, the polarization curve of W₁Mo₁-NG exhibits negligible differences compared with the initial curve after 10,000 even 50,000 CV cycles in 0.5 M H₂SO₄. Meanwhile, the polarization curves before and after 50,000 HER cycles in 1.0 M KOH also remain virtually unchanged (fig. S25). Furthermore, we performed aggressive long-term stability test on W₁Mo₁-NG by galvanostatic measurement at a current density of -10 mA cm⁻² at room temperature (25°C) (Fig. 5I). After 100,000 s, W₁Mo₁-NG DAC still retains 98% of the initial overpotential in 0.5 M H₂SO₄ and 95% in 1.0 M KOH solutions, respectively, higher than those of Pt/C with 93 and 82%. Again, to further study the effect of temperature on stability, W₁Mo₁-NG electrocatalyst was also verified by chronopotentiometric curves in 0.5 M H₂SO₄ and 1.0 M KOH solutions below (5°, 10°, 15°, and 20°C) and above (40°, 60°, 80°, and 90°C) room temperature. As exhibited in fig. S26, W₁Mo₁-NG exhibits substantially constant overpotentials over the temperature range 5° to 90°C for 100,000 s, highlighting the excellent stability over a wide temperature range. Besides, the XRD characterization reveals no evidence phase transition for W₁Mo₁-NG after cycling test (fig. S27). The chemical valence states of W and Mo ions remain almost unchanged, further signifying the robustness of the heteronuclear W₁Mo₁-NG catalyst (fig. S28). In particular, the HER activity of W₁Mo₁-NG DAC remains undegraded even storing for more than 2 years, confirming the remarkable chemical stability (fig. S29). The excellent physicochemical stability can be attributed to the robust W-O-Mo-O-C configuration with strong W-O and Mo-O bonds inherited from the W- and Mo-based POMs, respectively.

DFT calculation

To understand that the O-coordinated W_1Mo_1 -NG system promotes the catalytic reaction over wide range of pH 0 to pH 14, we performed the correlative theoretical calculations based on DFT studies. In general, the Gibbs free energy of hydrogen adsorption ($\Delta G_{\rm H}$) is a widely used descriptor to assess the activity of a catalyst for HER in both acidic and alkaline electrolytes (36). Here, a large amount of possible W-Mo, Mo₂, and W₂ dimer models were judiciously constructed by switching their coordinated O and N atoms while maintaining the metal centers unchanged. On the basis of EXAFS fitting results, the DFT geometry optimization indicates that the O-bridged W-Mo atoms are anchored in NG vacancies through oxygen atoms with W-O-Mo-O-C configuration in heteronuclear model of W₁Mo₁-NG, as shown in Fig. 6A, including all possible active sites, namely, O1, O2, C3, O4, O5, O6, O7, W8, and Mo9. While, for the homonuclear Mo2-NG and W2-NG models, atomic H adsorbs on terminal O atoms linked with metal centers (Fig. 6, B and C). We calculated $\Delta G_{\rm H}$ on the abovementioned sites for DACs, and the results are summarized in Fig. 6D and fig. S30. For heteronuclear W₁Mo₁-NG system, according to the Sabatier principle, we focused on six nonequivalent active sites: Mo-coordinated terminal O, O1; W-coordinated terminal O, O2; bridging oxygen in Mo-O-C motif, O4 and O5; bridging oxygen in Mo-O-W motif, O6; Mo-coordinated C, C3. Specifically, the bridged oxo in POMs is preferred for proton adsorption; thus, bridging oxygen in W-O-Mo-O-C configuration inherited from POMs shows optimal $\Delta G_{\rm H}$ in electrocatalytic HER. The $\Delta G_{\rm H}$ of these six nonmetal sites locates far optimal value than those of homonuclear Mo₂-NG and W₂-NG, implying that the heteronuclear W₁Mo₁-NG with diverse binding sites is more active than the homonuclear catalysts. Obviously, W₁Mo₁-NG system with six nonmetal sites guarantees optimal $\Delta G_{\rm H}$ throughout the entire pH range, indicating that W-O-Mo-O-C configuration could redistribute the electronic structure, which affords an improved electron environment for HER. In particular, the O1 site provides a low $\Delta G_{\rm H}$ of -0.065 eV, which is close to the optimal condition and even lower than that of commercial Pt catalyst (-0.10 eV). For O-coordinated W_1Mo_1 -NG DAC, ΔG_H can reach the optimal value (marked with dash line) at any pH, which is consistent with the electrochemical test results, suggesting that the unique O-coordinated W-Mo heterodimer is the active ingredient for HER under given pH condition. Moreover, when W-Mo heterodimers are coordinated with N atoms and tuned O/N atoms, the coordination environment of metal atoms is inconsistent with the EXAFS fitting and XPS results, and the corresponding W-O-Mo-N-C, W-N-Mo-N-C and W-O-Mo-(N, O)—C models show positive $\Delta G_{\rm H}$ from 1.760 to 2.347 eV with no H adsorption (fig. S31), further demonstrating the validity of the W—O—Mo—O—C model. In contrast, the experimentally determined O-coordinated Mo₂-NG and N-coordinated W₂-NG systems exhibit the $\Delta G_{\rm H}$ of -3.172 and -1.250 eV, respectively, indicating overbinding of H, thereby leading to the sites blocking. Furthermore, the other N/O-coordinated Mo₂ and W₂ homodimer configurations display $\Delta G_{\rm H}$ ranging from 1.09 to 2.278 eV (figs. S32 and S33), where the coordination of Mo and W atoms actually contradicts with the EXAFS fitting and XPS results, confirming the structural rationality of O-coordinated Mo₂-NG and N-coordinated W₂-NG models. Thus, according to the DFT calculation results, the O-coordinated W₁Mo₁-NG system has a near-optimum synergistic effect and gives more favorable ΔG_H for HER than O-coordinated Mo₂-NG and N-coordinated W2-NG systems as well as other Mo atom- and W atom-nucleated structures.

To investigate the electronic structure of W_1Mo_1 -NG DAC with improved HER activity, we perform the Bader charge analysis to quantitatively chemical analyze the differences among the DACs

(see Materials and Methods). The W₁Mo₁-NG, Mo₂-NG and W₂-NG systems give almost identical Bader charge value for O atom with 6.83 e. However, the O-coordinated W₁Mo₁-NG delivers a Bader volume of 291 pm³, which is much larger than those of Mo₂-NG (206.6 pm³) and W₂-NG (149.8 pm³). In addition, as shown in Fig. 6, E and F, electrons are delocalized in W₁Mo₁-NG system, well corresponding to the much larger Bader volume, indicating that the O-coordinated W-Mo heterodimer has strong covalent character with weak ionic property. Compared to heteronuclear W₁Mo₁-NG, the homonuclear Mo₂-NG and W₂-NG exhibit growing ionic nature because the electrons are strongly localized around coordination atoms (Fig. 6, G and H), via which the electrons from the metal centers are partially depleted to the coordinated O sites, leading to strong overbinding of H. Besides, the projected density of states (PDOS) on Mo, W, and O atoms was further performed to detect the electronic band structure of W₁Mo₁-NG. As illustrated in Fig. 6I, for three DAC systems, the Mo, W, and O atoms exhibit unoccupied states, deriving from the covalent bonding between metal ions and O atoms; the density of states (DOS) around the Fermi level (E_F) is dominated by O 2p orbital. Notably, heteronuclear W₁Mo₁-NG exhibits an increased DOS for the occupied states from 0.30 eV to the $E_{\rm F}$ (the shadowed part in Fig. 6I) due to the delocalized electrons (37), corresponding to the favorable adsorption behavior of H. Meanwhile, the delocalized electrons for W₁Mo₁-NG system can reduce the adsorption energy between the active sites and water in alkaline solution (37), which could lower the energetic barrier for the reorganization of the interfacial water network, thereby enhancing the hydrogen evolution rate (38). Besides, the results also suggest that W₁Mo₁-NG with delocalized electrons offers enhanced electrical conductivity compared to Mo₂-NG and W₂-NG, in accordance with EIS results (fig. S24). As a result, the distinctive W-O-Mo-O-C configuration with delocalized electrons ensures the optimal $\Delta G_{\rm H}$ and enhances reaction kinetics, thereby improving the HER activity in pH-universal electrolyte. In W₁Mo₁-NG system, the overlap of the electron clouds between W site and O site deforms the electron cloud of Mo site, and vice versa, which could cause distortion of the structure and electron redistribution, resulting in the electron delocalization of the W—O—Mo—O—C configuration (39). In addition, since the terminal O atom is the most promising active site, we extracted the bonding and antibonding states of H adsorbed on terminal O atom by projected crystal orbital Hamilton population (pCOHP) analysis. Fig. 6J displays the -pCOHP curves of the H-O coupling in the adsorption configurations. In O-coordinated W₁Mo₁-NG and Mo₂-NG systems, O 2s and O 2p_z valence orbitals are actively participating in the hybridization with H. The antibonding states of Mo₂-NG system (1.67 eV) move to higher energy level compared to W₁Mo₁-NG system (0.50 eV), indicating strong interaction with hydrogen (40), which corresponds to the excessive adsorption strength of Mo2-NG $(\Delta G_{\rm H} = -3.172 \text{ eV})$. Whereas, in N-coordinated W₂-NG system, the O 2p_x and O 2p_z valence orbitals are participating in the hybridization with H, which causes an antibonding state (0.40 eV) above the $E_{\rm F}$, ensuring strong interaction with hydrogen ($\Delta G_{\rm H} = -1.25 \; {\rm eV}$).

DISCUSSION

In summary, we have developed a facile two-step method to prepare the W₁Mo₁-NG DAC via a hydrothermal self-assembly of pHdependent POMs and GO, followed by CVD process. In W₁Mo₁-NG, O-coordinated W-Mo heterodimers are anchored in NG; W and Mo

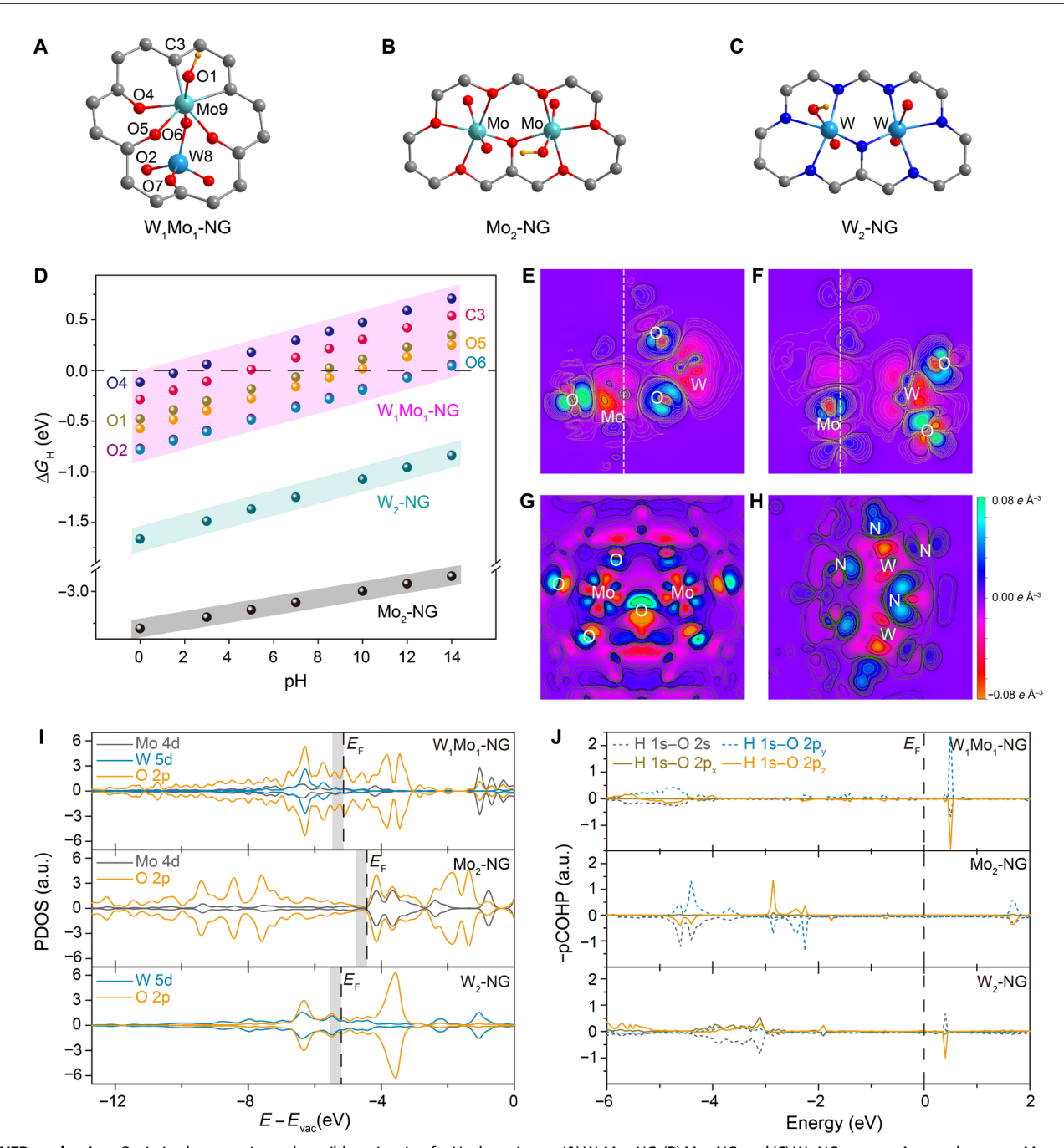


Fig. 6. HER mechanism. Optimized geometries and possible active sites for H adsorption on (**A**) W_1MO_1 -NG, (**B**) MO_2 -NG, and (**C**) W_2 -NG systems. Atom colors: cyan, MO_1 -NG is given by dark gray, C_1 ; blue, N_1 ; red, C_2 ; orange, C_3 ; h. (**C**) C_3 orange, C_4 ; blue, C_4 ; orange, C_4 ; blue, C_4 ; orange, C_4 ; blue, C_4 ; orange, C_4 ; orange, C_4 ; orange and C_4 ; orange density maps of heteronuclear C_4 ; orange and C_4 ; orange and aquamarine regions indicate electron depletion and accumulation, respectively. (**I**) Projected density of states (PDOS) of metal and C_4 ; orange an

atoms are respectively located in oxygen-bridged [WO₄] tetrahedron and distorted [MoO₆] octahedron. The distinctive W—O—Mo—O—C configuration is the active site for HER, which guarantees excellent catalytic activity and high stability. DFT results reveal that electron delocalization of W₁Mo₁-NG system affords the desirable $\Delta G_{\rm H}$ and good HER kinetics, thereby promoting HER activity. These results suggest that the self-assembly of POMs can be a versatile method for preparing atomic-scale catalysts with uniform distributed active ingredients.

MATERIALS AND METHODS

Materials synthesis

 $Na_2WO_4\cdot 2H_2O$ and $(NH_4)_6Mo_7O_{24}\cdot 4H_2O$ precursors were added to aqueous suspension of GO to form a homogeneous solution. Subsequently, the resulting mixture was transferred to a Teflon-lined autoclave and heated at 190°C for 12 hours. The as-prepared product was freeze-dried to produce a spongy column. Sponge column of p-RGO with O-coordinated W-Mo heterodimers was obtained by

freeze drying of the product after hydrothermal synthesis. Last, the nanocomposite was reacted with NH $_3$ /Ar at 800°C in a CVD apparatus to obtain Mo $_2$ -NG, W $_1$ Mo $_1$ -NG, W $_2$ -NG, and NG catalysts. The details are shown in the Supplementary Materials.

Materials characterization

A JEOL-JSM-7001F SEM and JEOL 2100 field emission gun TEM were used to examine the morphology. AC HAADF-STEM images and EDS elemental mappings were carried out by a Cs-corrected FEI Titan G2 60-300 equipped with a Super-X EDS detector and operated at 300 kV. Chemical compositions and elemental oxidation states were checked by XPS spectra (PHI-5702). X-ray absorption spectra (XANES and EXAFS) of W L₃- and Mo K-edges were measured on VESPERS beamline at the Canadian Light Source, by scanning a double-crystal Si(111) monochromator and collecting emitted x-ray fluorescence.

Computational details

The first-principles calculations based on the DFT were performed within spin-polarized generalized gradient approximation. Core electron states were represented by the projector augmented-wave method (41) as implemented in the Vienna ab initio simulation package (42). The Perdew-Burke-Ernzerhof (43) exchange correlation functional and a plane wave representation for the wave function with a cutoff energy of 450 eV were used. Lattice parameters and geometry of crystal were fully optimized on the basis of the criteria of a maximum atomic force of 0.01 eV Å⁻¹ and energy convergence criteria of 0.1 meV before the electron structure and total energy calculation. We adopted a single layer-doped graphene with 7×7 supercell model and chose the K-point mesh of $2 \times 2 \times 1$. The spin polarization was also switched on to account its effect, and 15Å vacuum layer was added to separate the graphene layers. The Bader charge analysis of the electron distribution was based on the usage of quantum theory of atoms in molecules method provided in VTST (44). The free energy of the H adsorption was calculated as

$$\Delta G_{\rm H} = E({\rm H}^*) + ZPE({\rm H}^*) - TS({\rm H}^*) - E(^*) - \frac{1}{2} [E({\rm H}_2) + ZPE({\rm H}_2) - TS({\rm H}_2)]$$
(1)

where asterisk means adsorption on the graphene substrate. The COHP analyses were performed by LOBSTER program [@Maintz16JCC37] (45).

SUPPLEMENTARY MATERIALS

Supplementary material for this article is available at http://advances.sciencemag.org/cgi/content/full/6/23/eaba6586/DC1

REFERENCES AND NOTES

- J. Shan, T. Ling, K. Davey, Y. Zheng, S.-Z. Qiao, Transition-metal-doped Rulr bifunctional nanocrystals for overall water splitting in acidic environments. *Adv. Mater.* 31, 1900510 (2019).
- C. C. Yang, S. F. Zai, Y. T. Zhou, L. Du, Q. Jiang, Fe₃C-Co nanoparticles encapsulated in a hierarchical structure of N-doped carbon as a multifunctional electrocatalyst for ORR, OER, and HER. Adv. Funct. Mater. 29, 1901949 (2019).
- H. Jin, X. Liu, A. Vasileff, Y. Jiao, Y. Zhao, Y. Zheng, S.-Z. Qiao, Single-crystal nitrogen-rich two-dimensional Mo₅N₆ nanosheets for efficient and stable seawater splitting. ACS Nano 12, 12761–12769 (2018).
- Y. Yu, G.-H. Nam, Q. He, X.-J. Wu, K. Zhang, Z. Yang, J. Chen, Q. Ma, M. Zhao, Z. Liu, F.-R. Ran, X. Wang, X. Huang, B. Li, Q. Xiong, Q. Zhang, Z. Liu, L. Gu, Y. Du, W. Huang, H. Zhang, High phase-purity 1T'-MoS₂- and 1T'-MoSe₂-layered crystals. *Nat. Chem.* 10, 638–643 (2018).

- J. Duan, S. Chen, C. A. Ortíz-Ledón, M. Jaroniec, S.-Z. Qiao, Phosphorus vacancies boost electrocatalytic hydrogen evolution by two orders of magnitude. *Angew. Chem. Int. Ed.* 10.1002/anie.201914967. (2020).
- X. Wei, Y. Zhang, H. He, D. Gao, J. Hu, H. Peng, L. Peng, S. Xiao, P. Xiao, Carbon-incorporated NiO/Co₃O₄ concave surface microcubes derived from a MOF precursor for overall water splitting. *Chem. Commun.* 55, 6515–6518 (2019).
- X. Wang, C. Xu, M. Jaroniec, Y. Zheng, S.-Z. Qiao, Anomalous hydrogen evolution behavior in high-pH environment induced by locally generated hydronium ions. Nat. Commun. 10, 4876 (2019).
- Y. Zhao, T. Ling, S. Chen, B. Jin, A. Vasileff, Y. Jiao, L. Song, J. Luo, S.-Z. Qiao, Non-metal single iodine atom electrocatalysts for the hydrogen evolution reaction. *Angew. Chem. Int. Ed.* 58, 12252–12257 (2019).
- E. C. Tyo, S. Vajda, Catalysis by clusters with precise numbers of atoms. Nat. Nanotechnol. 10, 577–588 (2015).
- S. Campisi, C. E. Chan-Thaw, A. Villa, Understanding heteroatom-mediated metalsupport interactions in functionalized carbons: A perspective review. *Appl. Sci.* 8, 1159 (2018)
- W. I. Choi, B. C. Wood, E. Schwegler, T. Ogitsu, Combinatorial search for high-activity hydrogen catalysts based on transition-metal-embedded graphitic carbons. *Adv. Energy Mater.* 5, 1501423 (2015).
- A. Grimaud, K. J. May, C. E. Carlton, Y.-L. Lee, M. Risch, W. T. Hong, J. Zhou, Y. Shao-Horn, Double perovskites as a family of highly active catalysts for oxygen evolution in alkaline solution. *Nat. Commun.* 4, 2439 (2013).
- L. Bai, C.-S. Hsu, D. T. L. Alexander, H. M. Chen, X. Hu, A cobalt-iron double-atom catalyst for the oxygen evolution reaction. J. Am. Chem. Soc. 141, 14190–14199 (2019).
- H. Zhang, P. Zhang, M. Qiu, J. Dong, Y. Zhang, X. W. Lou, Ultrasmall MoO_x clusters as a novel cocatalyst for photocatalytic hydrogen evolution. *Adv. Mater.* 31, 1804883 (2018)
- L. R. Radovic, B. Bockrath, On the chemical nature of graphene edges: Origin of stability and potential for magnetism in carbon materials. J. Am. Chem. Soc. 127, 5917–5927 (2005)
- A. Müller, F. Peters, M. T. Pope, D. Gatteschi, Polyoxometalates: Very large clustersnanoscale magnets. Chem. Rev. 98, 239–272 (1998).
- A. Rodríguez-Fortea, L. Vilà-Nadal, J. M. Poblet, Hydration of hydrogentungstate anions at different pH conditions: A car-parrinello molecular dynamics study. *Inorg. Chem.* 47, 7745–7750 (2008)
- L. Vilà-Nadal, A. Rodríguez-Fortea, L.-K. Yan, E. F. Wilson, L. Cronin, J. M. Poblet, Nucleation mechanisms of molecular oxides: A study of the assembly-dissassembly of [W₆O₁₉]²⁻ by theory and mass spectrometry. *Angew. Chem. Int. Ed.* 48, 5452–5456 (2009).
- D.-L. Long, P. Kögerler, L. J. Farrugia, L. Cronin, Restraining symmetry in the formation of small polyoxomolybdates: Building blocks of unprecedented topology resulting from "shrink-wrapping" [H₂Mo₁₆O₅₂]¹⁰⁻-type clusters. *Angew. Chem. Int. Ed.* 42, 4180–4183 (2003).
- Z. Luo, R. Miao, T. D. Huan, I. M. Mosa, A. S. Poyraz, W. Zhong, J. E. Cloud, D. A. Kriz, S. Thanneeru, J. He, Y. Zhang, R. Ramprasad, S. L. Suib, Mesoporous MoO_{3-x} material as an efficient electrocatalyst for hydrogen evolution reactions. *Adv. Energy Mater.* 6, 1600528 (2016).
- C. Guo, S. Yin, Q. Dong, T. Sato, Simple route to (NH₄)_xWO₃ nanorods for near infrared absorption. Nanoscale 4, 3394–3398 (2012).
- H. Yan, C. Tian, L. Wang, A. Wu, M. Meng, L. Zhao, H. Fu, Phosphorus-modified tungsten nitride/reduced graphene oxide as a high-performance, non-noble-metal electrocatalyst for the hydrogen evolution reaction. *Angew. Chem. Int. Ed.* 54, 6325–6329 (2015).
- 23. D. O. Scanlon, G. W. Watson, D. J. Payne, G. R. Atkinson, R. G. Egdell, D. S. L. Law, Theoretical and experimental study of the electronic structures of MoO_3 and MoO_2 . *J. Phys. Chem. C* **114**, 4636–4645 (2010).
- D. S. Dalavi, R. S. Devan, R. A. Patil, R. S. Patil, Y.-R. Ma, S. B. Sadale, I. Kim, J.-H. Kim, P. S. Patil, Efficient electrochromic performance of nanoparticulate WO₃ thin films. J. Mater. Chem. C 1, 3722–3728 (2013).
- H. Wang, S. Hamanaka, Y. Nishimoto, S. Irle, T. Yokoyama, H. Yoshikawa, K. Awaga, In operando x-ray absorption fine structure studies of polyoxometalate molecular cluster batteries: Polyoxometalates as electron sponges. J. Am. Chem. Soc. 134, 4918–4924 (2012)
- T. Ressler, J. Wienold, R. E. Jentoft, T. Neisius, Bulk structural investigation of the reduction of MoO₃ with propene and the oxidation of MoO₂ with oxygen. J. Catal. 210, 67–83 (2002).
- K. Okumura, T. Tomiyama, S. Shirakawa, S. Ishida, T. Sanada, M. Arao, M. Niwa, Hydrothermal synthesis and catalysis of Nb₂O₅-WO_x nanofiber crystal. *J. Mater. Chem.* 21, 229–235 (2011).
- L. Gracia, V. M. Longo, L. S. Cavalcante, A. Beltrán, W. Avansi, M. S. Li, V. R. Mastelaro, J. A. Varela, E. Longo, J. Andrés, Presence of excited electronic state in CaWO₄ crystals provoked by a tetrahedral distortion: An experimental and theoretical investigation. *J. Appl. Phys.* 110, 043501 (2011).

SCIENCE ADVANCES | RESEARCH ARTICLE

- W.-F. Chen, J. T. Muckermana, E. Fujita, Recent developments in transition metal carbides and nitrides as hydrogen evolution electrocatalysts. *Chem. Commun.* 49, 8896–8909 (2013)
- H.-J. Zhai, X. Huang, T. Waters, X.-B. Wang, R. A. J. O'Hair, A. G. Wedd, L.-S. Wang, Photoelectron spectroscopy of doubly and singly charged group VIB dimetalate anions M₂O₇²⁻, MM'O₇²⁻, and M₂O₇⁻ (M, M' = Cr, Mo, W). *J. Phys. Chem. A* 109, 10512–10520 (2005)
- Y. Lin, K. Sun, S. Liu, X. Chen, Y. Cheng, W.-C. Cheong, Z. Chen, L. Zheng, J. Zhang, X. Li, Y. Pan, C. Chen, Construction of CoP/NiCoP nanotadpoles heterojunction interface for wide pH hydrogen evolution electrocatalysis and supercapacitor. *Adv. Energy Mater.* 9, 1901213 (2019)
- X. Liu, W. Li, X. Zhao, Y. Liu, C.-W. Nan, L.-Z. Fan, Two birds with one stone: Metal–organic framework derived micro-/nanostructured Ni₂P/Ni hybrids embedded in porous carbon for electrocatalysis and energy storage. Adv. Funct. Mater. 29, 1901510 (2019).
- B. E. Conway, B. V. Tilak, Interfacial processes involving electrocatalytic evolution and oxidation of H₂, and the role of chemisorbed H. *Electrochim. Acta* 47, 3571–3594 (2002)
- M. A. R. Anjum, H. Y. Jeong, M. H. Lee, H. S. Shin, J. S. Lee, Efficient hydrogen evolution reaction catalysis in alkaline media by all-in-one MoS₂ with multifunctional active sites. Adv. Mater. 30, 1707105 (2018).
- B. You, Y. Zhang, Y. Jiao, K. Davey, S. Z. Qiao, Negative charging of transition-metal phosphides via strong electronic coupling for destabilization of alkaline water. *Anaew. Chem. Int. Ed.* 58, 11796–11800 (2019).
- N. Danilovic, R. Subbaraman, D. Strmcnik, V. R. Stamenkovic, N. Markovic, Electrocatalysis of the HER in acid and alkaline media. J. Serb. Chem. Soc. 78, 2007–2015 (2013).
- S. Chen, Z. Kang, X. Hu, X. Zhang, H. Wang, J. Xie, X. Zheng, W. Yan, B. Pan, Y. Xie, Delocalized spin states in 2D atomic layers realizing enhanced electrocatalytic oxygen evolution. *Adv. Mater.* 29, 1701687 (2017).
- I. Ledezma-Yanez, W. D. Z. Wallace, P. Sebastián-Pascual, V. Climent, J. M. Feliu, M. T. M. Koper, Interfacial water reorganization as a pH-dependent descriptor of the hydrogen evolution rate on platinum electrodes. *Nat. Energy* 2, 17031 (2017).
- K. Singh, S. Acharya, D. V. Atkare, Qualitative analysis of tolerance factor, electronegativity and chemical bonding of some ferroelectric perovskites through MOT. Ferroelectrics 315, 91–110 (2005).
- M. D. Hossain, Z. Liu, M. Zhuang, X. Yan, G.-L. Xu, C. A. Gadre, A. Tyagi, I. H. Abidi, C.-J. Sun, H. Wong, A. Guda, Y. Hao, X. Pan, K. Amine, Z. Luo, Rational design of graphenesupported single atom catalysts for hydrogen evolution reaction. *Adv. Energy Mater.* 9, 1803689 (2019).
- 41. P. E. Blöchl, Projector augmented-wave method. *Phys. Rev. B* **50**, 17953–17979 (1994).
- 42. J. Hafner, Ab-initio simulations of materials using VASP: Density-functional theory and beyond. *J. Comput. Chem.* **29**, 2044–2078 (2008).
- J. P. Perdew, K. Burke, M. Ernzerhof, Generalized gradient approximation made simple. Phys. Rev. Lett. 77, 3865–3868 (1996).
- 44. H. J. Bohórquez, R. J. Boyd, C. F. Matta, Molecular model with quantum mechanical bonding information. *J. Phys. Chem. A* **115**. 12991–12997 (2011).
- S. Maintz, V. L. Deringer, A. L. Tchougréeff, R. Dronskowski, LOBSTER: A tool to extract chemical bonding from plane-wave based DFT. J. Comput. Chem. 37, 1030–1035 (2016).
- D. C. Marcano, D. V. Kosynkin, J. M. Berlin, A. Sinitskii, Z. Sun, A. Slesarev, L. B. Alemany, W. Lu, J. M. Tour, Improved synthesis of graphene oxide. ACS Nano 4, 4806–4814 (2010).
- C.-Y. Yen, C.-H. Lee, Y.-F. Lin, H.-L. Lin, Y.-H. Hsiao, S.-H. Liao, C.-Y. Chuang, C.-C. M. Ma, Sol-gel derived sulfonated-silica/Nafion^{*} composite membrane for direct methanol fuel cell. *J. Power Sources* 173, 36–44 (2007).
- J.-H. Jung, J.-H. Jeon, V. Sridhar, I.-K. Oh, Electro-active graphene-Nafion actuators. Carbon 49, 1279–1289 (2011).
- J. Guo, J. Wang, Z. Wu, W. Lei, J. Zhu, K. Xia, D. Wang, Controllable synthesis of molybdenum-based electrocatalysts for a hydrogen evolution reaction. *J. Mater. Chem. A* 5, 4879–4885 (2017).
- B. Ma, Z. Yang, Y. Chen, Z. Yuan, Nickel cobalt phosphide with three-dimensional nanostructure as a highly efficient electrocatalyst for hydrogen evolution reaction in both acidic and alkaline electrolytes. *Nano Res.* 12, 375–380 (2019).
- 51. Y. Gong, L. Wang, H. Xiong, M. Shao, S. Zhuang, Y. Tang, X. Yang, Y. Chen, P. Wan, 3D self-supported Ni nanoparticle@N-doped carbon nanotubes anchored on NiMoN pillars

- for the hydrogen evolution reaction with high activity and anti-oxidation ability. *J. Mater. Chem. A* **7**, 13671–13678 (2019).
- H. Liu, X. Peng, X. Liu, G. Qi, J. Luo, Porous Mn-doped FeP/Co₃(PO₄)₂ nanosheets as efficient electrocatalysts for overall water splitting in a wide pH range. *ChemSusChem* 12, 1334–1341 (2019).
- G. Zhao, X. Wang, S. Wang, K. Rui, Y. Chen, H. Yu, J. Ma, S. X. Dou, W. Sun, Heteroatom-doped MoSe₂ nanosheets with enhanced hydrogen evolution kinetics for alkaline water splitting. *Chem. Asian J.* 14, 301–306 (2019).
- F. Guo, Y. Wu, X. Ai, H. Chen, G.-D. Li, W. Chen, X. Zou, A class of metal diboride electrocatalysts synthesized by a molten salt-assisted reaction for the hydrogen evolution reaction. *Chem. Commun.* 55. 8627–8630 (2019).
- Y. Hu, B. Yu, M. Ramadoss, W. Li, D. Yang, B. Wang, Y. Chen, Scalable synthesis
 of heterogeneous W–W₂C nanoparticle-embedded CNT networks for boosted hydrogen
 evolution reaction in both acidic and alkaline media. ACS Sustainable Chem. Eng. 7,
 10016–10024 (2019).
- H. Yan, Y. Xie, Y. Jiao, A. Wu, C. Tian, X. Zhang, L. Wang, H. Fu, Holey reduced graphene oxide coupled with an Mo₂N-Mo₂C heterojunction for efficient hydrogen evolution. *Adv. Mater.* 30, 1704156 (2018).
- R. Narasimman, M. Waldiya, E. Karthik, I. Mukhopadhyay, A. Ray, Transition metal dichalcogenide anchored in 3D nickel framework with graphene support for efficient electrocatalytic hydrogen evolution. *Adv. Sustainable Syst.* 3, 1800168 (2019).
- J. Wang, W. Yang, J. Liu, CoP₂ nanoparticles on reduced graphene oxide sheets as a super-efficient bifunctional electrocatalyst for full water splitting. *J. Mater. Chem. A* 4, 4686–4690 (2016).
- C. Wang, B. Tian, M. Wu, J. Wang, Revelation of the excellent intrinsic activity of MoS₂|NiS|MoO₃ nanowires for hydrogen evolution reaction in alkaline medium. ACS Appl. Mater. Interfaces 9, 7084–7090 (2017).
- T. Liu, X. Sun, A. M. Asiri, Y. He, One-step electrodeposition of Ni–Co–S nanosheets film as a bifunctional electrocatalyst for efficient water splitting. *Int. J. Hydrogen Energy* 41, 7264–7269 (2016).

Acknowledgments: We thank B. Chen from Rice University for assistance with XPS spectroscopy. We also acknowledge H. Fei at Hunan University and J. M. Tour from Rice University for valuable scientific discussion. We would also like to acknowledge J. Zhang from the Scientific Instrument Center at Shanxi University for her help with ICP-MS measurement. Funding: We acknowledge the National Natural Science Foundation of China (no. 21603129), Foundation of State Key Laboratory of Coal Conversion (grant no. J18-19-903), the Fund for Shanxi "1331" Project Key Innovative Research Team (1331KIRT, no. TD201704) the Program for the Outstanding Innovative Teams of Higher Learning Institutions of Shanxi (OIT), the Fund for Shanxi "1331" Project for Featured Discipline of Chemistry in SXNU for finance support of this research. The authors thank the support from Analytical Instrumentation Center (no. SPST-AIC10112914), SPST, ShanghaiTech University. Y.L. acknowledges the support by the National Science Foundation (no. 1900039) and the Welch Foundation (no. F-1959-20180324). Author contributions: Y.Y., Y.O., and X.F. conceived the experiment and scientific discussions. Y.Y. carried out the syntheses and electrocatalysis measurements. H.L., Z.Z., B.Z., Juncai Dong, W.Y., Jing Dong, and L.F. carried out the characterizations. R.F., J.Z., D.D., and P.Z. carried out the characterizations and provided the analysis. Y.L. and Y.M. carried out the computational investigation and provided the theoretical analysis. G.Y., Y.L., and X.Z. participated in the preparation of the manuscript. All authors discussed the results and revised the paper. Competing interests: The authors declare that they have no competing interests. Data and materials availability: All data needed to evaluate the conclusions in the paper are present in the paper and/or the Supplementary Materials. Additional data related to this paper may be requested from the authors.

Submitted 20 December 2019 Accepted 15 April 2020 Published 5 June 2020 10.1126/sciadv.aba6586

Citation: Y. Yang, Y. Qian, H. Li, Z. Zhang, Y. Mu, D. Do, B. Zhou, J. Dong, W. Yan, Y. Qin, L. Fang, R. Feng, J. Zhou, P. Zhang, J. Dong, G. Yu, Y. Liu, X. Zhang, X. Fan, O-coordinated W-Mo dual-atom catalyst for pH-universal electrocatalytic hydrogen evolution. *Sci. Adv.* 6, eaba6586 (2020).



O-coordinated W-Mo dual-atom catalyst for pH-universal electrocatalytic hydrogen evolution

Yang Yang, Yumin Qian, Haijing Li, Zhenhua Zhang, Yuewen Mu, David Do, Bo Zhou, Jing Dong, Wenjun Yan, Yong Qin, Li Fang, Renfei Feng, Jigang Zhou, Peng Zhang, Juncai Dong, Guihua Yu, Yuanyue Liu, Xianming Zhang and Xiujun Fan

Sci Adv **6** (23), eaba6586. DOI: 10.1126/sciadv.aba6586

ARTICLE TOOLS http://advances.sciencemag.org/content/6/23/eaba6586

SUPPLEMENTARY http://advances.sciencemag.org/content/suppl/2020/06/01/6.23.eaba6586.DC1

REFERENCES This article cites 59 articles, 0 of which you can access for free

http://advances.sciencemag.org/content/6/23/eaba6586#BIBL

PERMISSIONS http://www.sciencemag.org/help/reprints-and-permissions

Use of this article is subject to the Terms of Service